P H Y S I C A L R E V I E W L E T T E R S

Approaching the Post-Newtonian Regime with Numerical Relativity: A Compact-Object Binary Simulation Spanning 350 Gravitational-Wave Cycles

Béla Szilágyi,[1] Jonathan Blackman,[1] Alessandra Buonanno,[2,3] Andrea Taracchini,[2] Harald P. Pfeiffer,[4,5]
Mark A. Scheel,[1] Tony Chu,[6,4] Lawrence E. Kidder,[7] and Yi Pan[3]

[1]*TAPIR, Walter Burke Institute for Theoretical Physics, California Institute of Technology,
Pasadena, California 91125, USA*
[2]*Max Planck Institute for Gravitational Physics (Albert Einstein Institute),
Am Mühlenberg 1, Potsdam-Golm 14476, Germany*
[3]*Department of Physics, University of Maryland, College Park, Maryland 20742, USA*
[4]*Canadian Institute for Theoretical Astrophysics, 60 St. George Street, University of Toronto,
Toronto, Ontario M5S 3H8, Canada*
[5]*Canadian Institute for Advanced Research, 180 Dundas Street West, Toronto, Ontario M5G 1Z8, Canada*
[6]*Department of Physics, Princeton University, Jadwin Hall, Princeton, New Jersey 08544, USA*
[7]*Center for Radiophysics and Space Research, Cornell University, Ithaca, New York 14853, USA*

We present the *first* numerical-relativity simulation of a compact-object binary whose gravitational waveform is long enough to cover the *entire* frequency band of advanced gravitational-wave detectors, such as LIGO, Virgo, and KAGRA, for mass ratio 7 and total mass as low as $45.5 M_\odot$. We find that effective-one-body models, either *uncalibrated* or *calibrated* against substantially shorter numerical-relativity waveforms at smaller mass ratios, reproduce our new waveform remarkably well, with a negligible loss in detection rate due to modeling error. In contrast, post-Newtonian inspiral waveforms and existing calibrated phenomenological inspiral-merger-ringdown waveforms display greater disagreement with our new simulation. The disagreement varies substantially depending on the specific post-Newtonian approximant used.

Introduction.—The upgraded ground-based interferometric gravitational-wave (GW) detectors LIGO [1,2] and Virgo [3] will begin scientific observations in mid 2015 and are expected to reach design sensitivity by 2019 [4]. Furthermore, a new Japanese detector KAGRA [5] is under construction. Direct detection of GWs by the end of this decade is, therefore, very likely. The most promising GW sources are compact-object binaries, wherein each partner is either a stellar-mass black hole (BH) or a neutron star (NS) [6]. The detection of GWs from compact-object binaries, as well as the determination of source properties from detected GW signals, relies on the accurate knowledge of the expected gravitational waveforms via matched-filtering [7] and Bayesian methods [8].

The need for accurate waveforms has motivated intense research. Early waveform models based on the post-Newtonian (PN) formalism [9] were limited to the early inspiral. The effective-one-body (EOB) formalism [10,11] extended waveform models to the late inspiral, merger, and ringdown. Since 2005, research has greatly benefited from numerical-relativity (NR) simulations [12–14]. (Besides its importance for GW astronomy, NR has also deepened the understanding of general relativity in topics such as binary BH recoil [15,16], gravitational self-force [17], high-energy physics, and cosmology [18,19].) Current inspiral-merger-ringdown (IMR) waveform models [20–23]

combine information from analytical-relativity (AR) calculations (best suited for the inspiral, when comparable-mass binaries have characteristic velocities smaller than the speed of light) and direct NR simulations (the best means to explore the late inspiral and the merger).

However, there is a gap between the portion of the binary evolution that is described by analytical methods and the portion that is accessible by NR. For example, waveforms computed at the currently known PN order become unreliable possibly hundreds of orbits before merger for unequal-mass binaries [24,25] and even earlier when one of the objects is spinning [26]. [Several PN waveforms (or approximants) with different PN-truncation error are available in the literature. These PN approximants can differ from each other during the last hundreds of cycles before merger.] Yet NR simulations have been able to cover only tens of orbits [27–29] until now. This gap has emerged as one of the most important sources of uncertainty in present IMR waveform models. It is possible to construct IMR models by extending analytical waveforms across the gap [20–23], in some cases, obtaining IMR models that are faithful to longer numerical waveforms when extrapolated beyond their limited range of calibration [30]. However, so far these procedures have been tested using NR simulations with only 30 orbits, too few to close the gap.

The time duration T of an inspiral waveform starting at initial GW frequency f_{ini} scales as $T \propto \nu^{-1} f_{ini}^{-8/3}$, where $\nu = m_1 m_2 / M^2$ is the symmetric mass ratio of the binary with component masses $m_{1,2}$ and total mass $M = m_1 + m_2$. Therefore, reducing f_{ini} by a factor of 2 increases T sevenfold. Halving the symmetric mass ratio ν (e.g., from $m_1/m_2 = 2$ to $m_1/m_2 = 7$) doubles T. Increasing the simulation length T is difficult: it becomes harder to preserve phase coherency, the outer boundary of a simulation is in causal contact for a larger fraction of the simulation, and existing codes would require many months or even years of wall-clock time. Therefore, progress toward longer simulations has been sluggish, with T increasing by only about a factor of 2 to 3 during the last five years [28,29,31–33]. The duration T needed to close the gap depends on the binary parameters and the detector bandwidth. Here we start addressing the issue of the gap by focusing on the nonspinning case and high mass ratio, $q = m_1/m_2 = 7$, for which the PN approximants can greatly differ [25,34]. We present a new NR simulation that extends T by a factor of 20 and reduces the initial frequency f_{ini} by a factor of 3. With its comparatively high mass ratio, the new simulation probes an astrophysically relevant parameter regime for BH-BH and NS-BH binaries and for certain total masses covers the entire frequency band of advanced LIGO (aLIGO) and Virgo. We describe challenges involved in carrying out this new simulation, most notably, an unexpected motion of the binary center of mass (c.m.), and we suggest improvements for future long simulations. We then compare the new simulation with existing analytical waveform models to assess the impact of waveform model errors on the detection rate of advanced detectors.

Numerical-relativity waveforms.—We report on two new simulations of a nonspinning BH binary with mass ratio $q = m_1/m_2 = 7$. The *short* simulation is of typical length: 20 orbits, $T = 4,100M$. The *long* simulation, the main focus of this paper, is about 25 times longer. Both simulations are computed using the Spectral Einstein Code (SpEC) [35]. The short simulation uses established computational techniques [28]. The speed-up needed for the long simulation is the result of a series of code changes including task-based adaptive parallel load balancing, live timing-based selection of the most efficient algorithm (when multiple implementations of the same function are available), a modified memory layout to allow more efficient calls to low-level numerical packages, and a more efficient implementation of the generalized harmonic evolution equations. The highest resolution of the long simulation required 265 days on 48 cores. Figure 1 shows the new long waveform, and Table I presents additional details about both simulations. Geometrized units $G = c = 1$ are used in Table I and throughout this paper. The top inset of Fig. 1 shows the spectra of the (2,2) spherical-harmonic waveform modes. The long simulation covers the
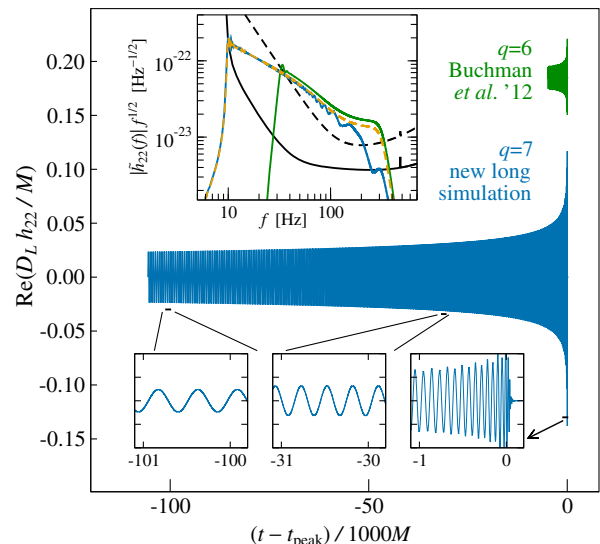

FIG. 1 (color online). Overview of the new very long simulation. The main panel shows the (2,2) spherical-harmonic mode of the GW strain, with enlargements in the lower insets. The top inset shows the Fourier spectra of the new waveform in blue and the NR-NR hybrid waveform (used for comparisons with analytical models) in yellow, overlaid with noise power-spectral densities of aLIGO at the early (dashed black) and design (solid black) sensitivity [4]. The waveforms in the inset are scaled to total mass $M = 45.5 M_\odot$ and luminosity distance $D_L \approx 1.06$ Gpc. For comparison, an older $q = 6$ waveform [27] of representative length is shown in the main panel (offset vertically for clarity) and in the power-spectrum inset.

entire design-aLIGO frequency range for nonspinning BH-BH binaries with $M \gtrsim 45 M_\odot$ and covers the early-aLIGO frequency range for $M \gtrsim 11 M_\odot$, including nonspinning NS-BH binaries. (For mass ratio 7, in absence of spin, we expect no observable differences in the merger signal between a BH-BH and a NS-BH binary [36].) In contrast, the $q = 6$ simulation plotted in green, which is representative of past simulations, starts at 3 times higher frequency, and covers a much smaller portion of the aLIGO bandwidth for a given M. Thus, we present here the first gravitational waveform covering the entire design-aLIGO frequency band for a nonspinning, compact-object binary at mass ratio $q = 7$ with a total mass as low as $M = 45.5 M_\odot$.

The short simulation is run at three different numerical resolutions and the long one at four resolutions. The long simulation employs dynamical spectral adaptive mesh refinement [37], so measured quantities (like BH masses or waveforms) do not always converge in a regular, predictable manner with increasing resolution, as is the case when each resolution is defined by a fixed number of grid points. Furthermore, failure to resolve initial transients caused by imperfect initial data also complicates convergence (see discussion in Sec. IIIB of Ref. [38]). Nevertheless, we find that differences in measured quantities like waveforms, masses, and spins decrease rapidly

TABLE I. Properties of the two NR simulations: The first block lists initial separation D_0, orbital frequency Ω_0, radial velocity $\dot{a}_0$, ADM energy E_{ADM}, and angular momentum J_{ADM} in units of total mass $M = m_1 + m_2$. The middle block lists mass ratio m_1/m_2, eccentricity ε, time duration T, and number of orbits N until merger. The final block lists remnant mass M_f and spin S_f.

Initial data					Inspiral				Remnant properties	
D_0/M	$10^3 M\Omega_0$	$10^6 \dot{a}_0 M$	E_{ADM}/M	J_{ADM}/M^2	m_1/m_2	$10^5\varepsilon$	T/M	N	M_f/M	S_f/M_f^2
12.2	21.1541	−47.99	0.996 211	0.4510	6.999 97(2)	<6	4,100	20	0.987 71(1)	0.328 30(3)
27	6.7930	0	0.998 112	0.6123	7.000 00(1)	34	106 000	176	0.987 62(14)	0.328 27(2)

with resolution, and Table I displays a conservative error estimate obtained by taking the difference between the two highest resolutions. After the initial transients have decayed, we measure the mass ratio to be equal to 7 to within five significant digits and the dimensionless spins to be $\lesssim 10^{-6}$. The remnant mass and spin agree to within four significant digits between the short and long simulations.

However, the long simulation encounters an unexpected problem. After a few $10000M$ of evolution, the coordinate c.m. begins to drift away from the origin. We define the c.m. as $\vec{c}_{c.m.} = \vec{c}_1 m_1/M + \vec{c}_2 m_2/M$, where $\vec{c}_{1,2}$ are the coordinate centers of the apparent horizons of the two BHs. Figure 2 shows that $|\vec{c}_{c.m.}|$ increases *exponentially* with time. This drift is primarily a coordinate effect that only marginally affects most measurable quantities. For example, the linear momentum radiated to infinity, as computed from the waveform obtained by Cauchy-characteristic extraction [39], is consistent with PN theory and is too small to account for the motion of the c.m. To explore the drift in more detail, we repeat the long simulation with different values of R, the coordinate radius of the artificial

FIG. 2 (color online). Top left: displacement of the c.m. from the origin for three long simulations with different outer boundary radii R. In each case, $|\vec{c}_{c.m.}|$ increases exponentially. Top right: growth rate σ of $|\vec{c}_{c.m.}|$ as a function of R with a power-law fit. Lower panels: GW (2,2) mode of the short and long simulations. The long simulation still agrees very well with the short one at early times but fails to produce an accurate merger waveform.

outer boundary where we impose an outgoing-wave boundary condition. The top left panel of Fig. 2 shows the c.m. drift for several values of R. Empirically, we find that the exponential growth rate σ behaves like $\sigma \propto R^{-1.45}$, cf. Fig. 2. For our standard choice of $R = 864M$, $1/\sigma = 26000M$; this large time scale explains why the drift was not noticed in earlier, shorter simulations.

We conjecture that the drift is caused by a coupling with the outer boundary. Such a coupling might arise through enhanced reflections of the outgoing GW at the outer boundary. Our outgoing-wave boundary conditions [40] have the smallest reflection coefficient for spherical-harmonic modes with small ℓ and a reflection coefficient of order unity when $kR/\ell \gtrsim 1$ [40], where k is the radial wave vector. With increasing $|\vec{c}_{c.m.}|$, the emitted GW will have increasing high-ℓ content when decomposed on the outer boundary.

From the bottom panel in Fig. 2, we see that the effects of the drift on the long waveform is confined to the last ~10 orbits before merger. In the Fourier domain (see Fig. 1), one can clearly see the unusual behavior of the long waveform at high frequencies. Since these orbits are covered by the short waveform, we hybridize the short waveform with the long one, thus, replacing the final portion of the former. We adopt the hybridization method of Ref. [41]. We construct nine NR-NR hybrids by combining three versions of the long simulation and three versions of the short simulation. Each version may differ by the numerical resolution (which we label by "Lev$\mathcal{N}$," where the adaptive mesh refinement aims for truncation errors $\propto e^{-\mathcal{N}}$) or by the degree of the polynomial used to extrapolate the waveform to infinity [39,42] (which we label by "$N\mathcal{M}$," where $\mathcal{M}$ is the polynomial degree.) For example, the Lev3 simulation uses ~90^3 collocation points near merger. In particular, we use (Lev3, $N3$), (Lev3, $N2$), and (Lev2, $N3$) for the long simulation, while we use (Lev5, $N3$), (Lev5, $N2$), and (Lev4, $N3$) for the short simulation. The fiducial NR-NR hybrid is built from the long (Lev3, $N3$) and the short (Lev5, $N3$) simulations; this pair of waveforms is blended over the interval $t - t_{peak} \in [-3252, -2252]M$. In the top panel of Fig. 1, we show in yellow the spectrum of the fiducial NR-NR hybrid. This spectrum behaves as expected close to merger and is devoid of oscillations, just like the spectrum of the $q = 6$ simulation. Since we cannot estimate the impact of the coordinate drift on the phase error of the
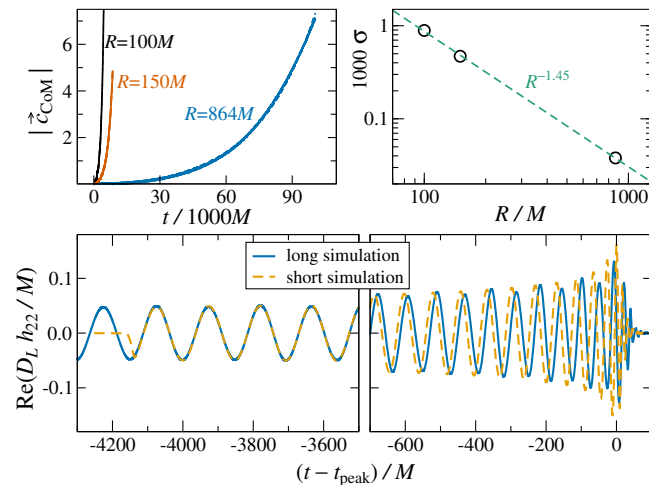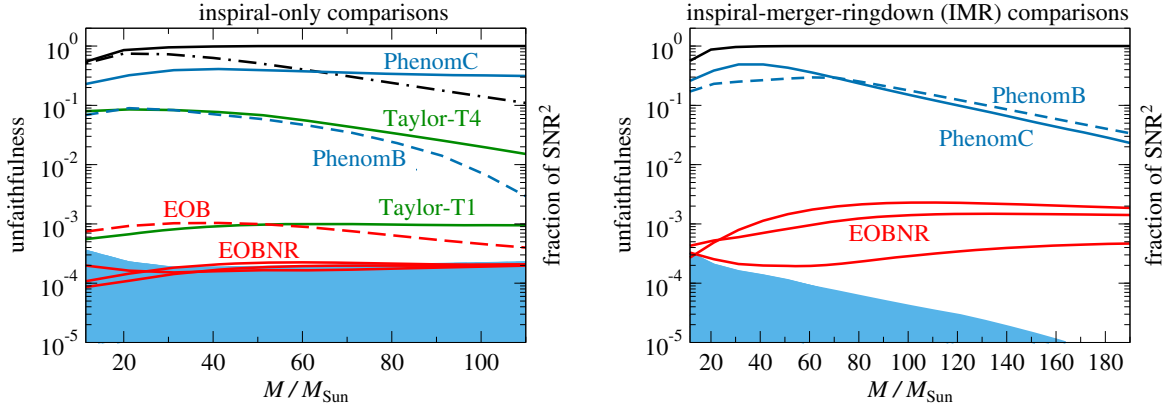
FIG. 3 (color online). Unfaithfulness of the hybrid NR-NR waveform against analytical models. Left: inspiral-only comparisons. Right: IMR comparisons. Also shown in the left panel are $\mathrm{SNR}^2_{\mathrm{insp}}/\mathrm{SNR}^2_{\mathrm{full-insp}}$ (solid black line) and $\mathrm{SNR}^2_{\mathrm{insp}}/\mathrm{SNR}^2_{\mathrm{full-IMR}}$ (dot-dashed black line), and in the right panel $\mathrm{SNR}^2_{\mathrm{IMR}}/\mathrm{SNR}^2_{\mathrm{full-IMR}}$ (solid black line). The blue area indicates the NR error. We note that the "EOB curve" does not use any information from NR simulations and the "EOBNR curves" were calibrated to other, much shorter NR waveforms with $q \neq 7$, but not to the NR waveforms of this paper.

long waveform, we cannot make statements about the phase disagreement between the long waveform and analytical waveform models. Nevertheless, we can compare the analytical models to the hybrid NR-NR waveform and investigate how the results change when we vary the blending window where the hybridization is done.

Comparison to analytical-relativity waveforms.— Figure 3 summarizes our comparisons between various analytical waveforms h^{AR}_{22} with the hybrid NR-NR waveform h^{NR}_{22}. Shown is the unfaithfulness $\bar{\mathcal{F}}$ defined as $\bar{\mathcal{F}} \equiv 1 - \max_{t_0,\phi_0}\langle h^{\mathrm{AR}}_{22}, h^{\mathrm{NR}}_{22}\rangle/\|h^{\mathrm{AR}}_{22}\|/\|h^{\mathrm{NR}}_{22}\|$. Here, t_0 and ϕ_0 are the initial time and phase, $\|h\| \equiv \sqrt{\langle h, h\rangle}$, and $\langle h_1, h_2\rangle \equiv 4\mathrm{Re}\int_{f_{\min}}^{f_{\max}} \tilde{h}_1(f)\tilde{h}^*_2(f)/S_n(f)df$, where $S_n(f)$ is the zero-detuned, high-power noise power-spectral density of aLIGO [43]. We consider the following analytical waveform models from the LIGO Algorithm Library (LAL): the inspiral-only PN Taylor approximants [44] in the time domain (Taylor-$T1$, $T2$, $T4$) and in the frequency domain (Taylor-$F2$), an inspiral EOB model (obtained from Ref. [23] by dropping any NR information, thus, uncalibrated), the IMR EOBNR models that were obtained by calibrating the EOB model to NR simulations [23,45,46] (denoted in LAL as EOBNRv2, SEOBNRv1, and SEOBNRv2), and the IMR phenomenological models that were built combining PN and NR results [20,21] (denoted in LAL as PhenomB and PhenomC). All the time-domain IMR waveforms are tapered using a Planck windowing function [47] both at the beginning and at the end. We generate the model waveforms from an initial GW frequency of $M\omega_{22} = 0.01317$ and use $f_{\min} = 12\,\mathrm{Hz}(45.5M_\odot/M)$. For inspiral-only models, we set $f_{\max} = 52.5\,\mathrm{Hz}(45.5M_\odot/M)$, the minimum available final GW frequency among the time-domain Taylor models, a value close to the innermost-circular-orbit value in Schwarzschild spacetime [$\approx 48.3\,\mathrm{Hz}(45.5M_\odot/M)$],

whereas for the IMR comparisons, $f_{\max} = \infty$. Quite interestingly, the inspiral-only comparisons give similar results when employing directly the long simulation instead of the NR-NR hybrid.

The blue shaded area in Fig. 3 represents the uncertainty in the NR waveforms estimated by computing $\bar{\mathcal{F}}$ between the fiducial hybrid NR-NR waveform and the other eight NR-NR hybrids. Because the inspiral-only and IMR curves are calculated using different portions of the hybrid NR-NR waveform, the same model may have different values in the two panels for the same total mass. We vary the prescriptions used for the hybridization (namely, position and width of the blending window), and we find changes $O(10^{-4})$ in the unfaithfulness curves for low total masses. Thus, we consider our results robust. If general relativity correctly describes the GW signals found in nature, then the unfaithfulness $\bar{\mathcal{F}}$ plotted in Fig. 3 yields a bound on the loss in detection rate due to modeling error. For sources uniformly distributed in space, the relative loss in detection rate is $\sim 3(d_{\mathrm{MM}} + d_E)$ (see Sec. VB in Ref. [44]), where d_{MM} is the minimal match of the template bank and $d_E = 1 - \max_{\vec{\lambda}}\langle h^{\mathrm{AR}}_{22}, h^{\mathrm{NR}}_{22}\rangle/\|h^{\mathrm{AR}}_{22}\|/\|h^{\mathrm{NR}}_{22}\|$ is the ineffectualness. Here, $\vec{\lambda}$ describes *all* the binary parameters not just ϕ_0 and t_0, and, therefore, $d_E \leq \bar{\mathcal{F}}$. Typically, $d_{\mathrm{MM}} = 3\%$ in LIGO searches. Thus, to achieve $\lesssim 10\%$ loss in detection rate, it suffices that $\bar{\mathcal{F}} \lesssim 1\%$ [44].

Quite remarkably, we find that the unfaithfulness of the uncalibrated *inspiral* EOB waveform is $< 0.1\%$, with a negligible loss in detection rate due to modeling error. The agreement is, of course, better for the inspiral EOBNR waveforms (i.e., EOBNRv2, SEOBNRv1, SEOBNRv2) ($\bar{\mathcal{F}} < 0.02\%$, left panel) and $\bar{\mathcal{F}} < 0.2\%$ for the IMR EOBNR waveforms (right panel). The closeness of all inspiral EOBNR waveforms strongly suggests that the different calibrations and variations in the dynamics and

energy fluxes of those EOBNR models [23,45,46] do not impact the low-frequency part of the waveforms but affect (in a minor way) only the last stages of the inspiral and the merger. The unfaithfulness of the time- and frequency-domain inspiral-only PN Taylor approximants varies between 0.1% and 10% depending on the binary's total mass and the PN approximant used. (The large unfaithfulness of some of the PN Taylor approximants is due to differences in the evolution of the frequency and its first time derivative during the late inspiral phase.) In particular, Taylor-$T4$, which has the best agreement with NR in the equal-mass case [33], has the largest disagreement with the new long $q = 7$ NR waveform. (The approximants Taylor-$T2$ and Taylor-$F2$ are not displayed but lie between Taylor-$T1$ and Taylor-$T4$.) The PhenomB and C models were fitted to hybrids built with Taylor PN approximants and less accurate, short NR waveforms, which may in part explain the large disagreement we find.

The new long NR waveform covers the entire design-aLIGO frequency band only for total mass $M \geq 45.5M_\odot$; for smaller M, the unfaithfulness calculations in Fig. 3 neglect the lowest-frequency portion of the waveform visible to aLIGO, down to ∼10 Hz. To understand the significance of the missing GW cycles in the low-frequency portion of the bandwidth, we compute the signal-to-noise ratio (SNR) accumulated within the frequency range $f_{min} \leq f \leq f_{max}$ (SNR_{insp} and SNR_{IMR} for the left and right panels of Fig. 3, respectively) and compare it with the SNR accumulated over the *entire* inspiral ($SNR_{full-insp}$) and the *entire* IMR ($SNR_{full-IMR}$), i.e., down to 10 Hz. To cover the entire design-aLIGO bandwidth, we use the calibrated EOB model of Ref. [23]. Suitable (squared) ratios of these quantities, which represent the fraction of total SNR that is accessible to our comparisons, are plotted in Fig. 3. These ratios are <1 whenever GW cycles are missing in the range 10 Hz $\leq f \leq f_{min}$ or, in the case of $SNR_{insp}^2/SNR_{full-IMR}^2$, also when the merger-ringdown signal is in band. We find that, even for total masses <$45.5M_\odot$, the unfaithfulness can still be a meaningful assessment of the quality of the analytical models, since a large fraction of SNR is accumulated. Because the merger-ringdown portion of the waveforms becomes increasingly important at higher masses, the inspiral-only comparisons at high mass cover only a small fraction of the entire SNR, as illustrated by the steep decline of $SNR_{insp}^2/SNR_{full-IMR}^2$ in the left panel of Fig. 3.

Conclusions.—To detect and extract unique, astrophysical information from coalescing compact-object binaries, GW instruments employ model waveforms built by combining analytical and numerical-relativity predictions [20–23]. Currently, the main uncertainty of those waveform models is caused by the gap between the regimes of applicability of those methods. This uncertainty can be addressed and, eventually, solved by running much longer NR simulations. In this work, we start to tackle this issue by

producing a BH-BH simulation 20 times longer than previous simulations. Because of an unexpected drift of the c.m. during the last 40 GW cycles, we construct the full NR inspiral, merger, and ringdown waveform by hybridizing the long NR waveform with a new, short NR simulation. The hybrid NR-NR waveform covers the entire band of advanced GW detectors for total mass $\geq 45.5M_\odot$. Comparing to analytical waveform models, we find strong evidence that—at least for nonspinning binaries—the EOB formalism accurately describes the inspiral dynamics in the so-far unexplored regime of 20 to 176 orbits before merger, and combined with previous work [30] provides accurate waveforms beyond the limited range of calibration. Quite remarkably, the excellent agreement of EOBNR waveforms from Refs. [23,45,46] holds also for inspiral EOB waveforms at 4PN order [23], obtained by dropping any information from NR simulations. PN approximants have larger errors, and, more important, the errors vary substantially depending on the specific PN approximant used.

[1] G. M. Harry (LIGO Scientific Collaboration), Classical Quantum Gravity **27**, 084006 (2010).
[2] LIGO Scientific Collaboration, Classical Quantum Gravity **32**, 074001 (2015).
[3] F. Acernese *et al.*, Classical Quantum Gravity **32**, 024001 (2015).
[4] J. Aasi *et al.* (LIGO Scientific Collaboration, Virgo Collaboration), arXiv:1304.0670.

[5] K. Somiya (KAGRA Collaboration), Classical Quantum Gravity **29**, 124007 (2012).

[6] J. Abadie *et al.* (LIGO Scientific Collaboration), Classical Quantum Gravity **27**, 173001 (2010).

[7] L. S. Finn and D. F. Chernoff, Phys. Rev. D **47**, 2198 (1993).

[8] J. Veitch *et al.*, Phys. Rev. D **91**, 042003 (2015).

[9] L. Blanchet, Living Rev. Relativity **9**, 4 (2006).

[10] A. Buonanno and T. Damour, Phys. Rev. D **59**, 084006 (1999).

[11] A. Buonanno and T. Damour, Phys. Rev. D **62**, 064015 (2000).

[12] F. Pretorius, Phys. Rev. Lett. **95**, 121101 (2005).

[13] M. Campanelli, C. O. Lousto, P. Marronetti, and Y. Zlochower, Phys. Rev. Lett. **96**, 111101 (2006).

[14] J. G. Baker, J. Centrella, D.-I. Choi, M. Koppitz, and J. van Meter, Phys. Rev. Lett. **96**, 111102 (2006).

[15] M. Campanelli, C. O. Lousto, Y. Zlochower, and D. Merritt, Phys. Rev. Lett. **98**, 231102 (2007).

[16] J. A. González, U. Sperhake, B. Brügmann, M. Hannam, and S. Husa, Phys. Rev. Lett. **98**, 091101 (2007).

[17] A. Le Tiec, A. Buonanno, A. H. Mroué, H. P. Pfeiffer, D. A. Hemberger, G. Lovelace, L. E. Kidder, M. A. Scheel, B. Szilagy, N. W. Taylor, and S. A. Teukolsky, Phys. Rev. D **88**, 124027 (2013).

[18] V. Cardoso, L. Gualtieri, C. Herdeiro, and U. Sperhake, arXiv:1409.0014.

[19] M. W. Choptuik, L. Lehner, and F. Pretorius, arXiv:1502.06853.

[20] P. Ajith, M. Hannam, S. Husa, Y. Chen, B. Brügmann, N. Dorband, D. Müller, F. Ohme, D. Pollney, C. Reisswig, L. Santamaría, and J. Seiler, Phys. Rev. Lett. **106**, 241101 (2011).

[21] L. Santamaría, F. Ohme, P. Ajith, B. Brügmann, N. Dorband, M. Hannam, S. Husa, P. Mösta, D. Pollney, C. Reisswig, E. L. Robinson, J. Seiler, and B. Krishnan, Phys. Rev. D **82**, 064016 (2010).

[22] T. Damour, A. Nagar, and S. Bernuzzi, Phys. Rev. D **87**, 084035 (2013).

[23] A. Taracchini, A. Buonanno, Y. Pan, T. Hinderer, M. Boyle, D. A. Hemberger, L. E. Kidder, G. Lovelace, A. H. Mroue, H. P. Pfeiffer, M. A. Scheel, B. Szilagyi, N. W. Taylor, and A. Zenginoglu, Phys. Rev. D **89**, 061502(R) (2014).

[24] T. Damour, A. Nagar, and M. Trias, Phys. Rev. D **83**, 024006 (2011).

[25] I. MacDonald, A. H. Mroué, H. P. Pfeiffer, M. Boyle, L. E. Kidder, M. A. Scheel, B. Szilágyi, and N. W. Taylor, Phys. Rev. D **87**, 024009 (2013).

[26] A. H. Nitz, A. Lundgren, D. A. Brown, E. Ochsner, D. Keppel, and I. W. Harry, Phys. Rev. D **88**, 124039 (2013).

[27] L. T. Buchman, H. P. Pfeiffer, M. A. Scheel, and B. Szilágyi, Phys. Rev. D **86**, 084033 (2012).

[28] A. H. Mroue, M. A. Scheel, B. Szilagyi, H. P. Pfeiffer, M. Boyle, D. A. Hemberger, L. E. Kidder, G. Lovelace, S. Ossokine, N. W. Taylor, A. Zenginoglu, L. T. Buchman, T. Chu, E. Foley, M. Giesler, R. Owen, and S. A. Teukolsky, Phys. Rev. Lett. **111**, 241104 (2013).

[29] I. Hinder *et al.* (NRAR Collaboration), Classical Quantum Gravity **31**, 025012 (2013).

[30] Y. Pan, A. Buonanno, A. Taracchini, M. Boyle, L. E. Kidder, A. H. Mroué, H. P. Pfeiffer, M. A. Scheel, B. Szilágyi, and A. Zenginoglu, Phys. Rev. D **89**, 061501 (R) (2014).

[31] B. Aylott, J. G. Baker, W. D. Boggs, M. Boyle, P. R. Brady *et al.*, Classical Quantum Gravity **26**, 165008 (2009).

[32] P. Ajith, M. Boyle, D. A. Brown, B. Brugmann, L. T. Buchman *et al.*, Classical Quantum Gravity **29**, 124001 (2012).

[33] M. Boyle, D. A. Brown, L. E. Kidder, A. H. Mroué, H. P. Pfeiffer, M. A. Scheel, G. B. Cook, and S. A. Teukolsky, Phys. Rev. D **76**, 124038 (2007).

[34] T. Damour, B. R. Iyer, and B. S. Sathyaprakash, Phys. Rev. D **63**, 044023 (2001).

[35] http://www.black-holes.org/SpEC.html.

[36] F. Foucart, L. Buchman, M. D. Duez, M. Grudich, L. E. Kidder, I. MacDonald, A. Mroue, H. P. Pfeiffer, M. A. Scheel, and B. Szilagyi, Phys. Rev. D **88**, 064017 (2013).

[37] B. Szilágyi, Int. J. Mod. Phys. D **23**, 1430014 (2014).

[38] M. A. Scheel, M. Giesler, D. A. Hemberger, G. Lovelace, K. Kuper, M. Boyle, and B. Szilágyi, Classical Quantum Gravity **32**, 105009 (2015).

[39] N. W. Taylor, M. Boyle, C. Reisswig, M. A. Scheel, T. Chu, L. E. Kidder, and B. Szilágyi, Phys. Rev. D **88**, 124010 (2013).

[40] L. T. Buchman and O. C. A. Sarbach, Classical Quantum Gravity **23**, 6709 (2006).

[41] I. MacDonald, S. Nissanke, and H. P. Pfeiffer, Classical Quantum Gravity **28**, 134002 (2011).

[42] M. Boyle and A. H. Mroué, Phys. Rev. D **80**, 124045 (2009).

[43] D. Shoemaker (LIGO Collaboration), LIGO Report No. T0900288-v3, 2010 https://dcc.ligo.org/LIGO-T0900288/public.

[44] A. Buonanno, B. R. Iyer, E. Ochsner, Y. Pan, and B. S. Sathyaprakash, Phys. Rev. D **80**, 084043 (2009).

[45] Y. Pan, A. Buonanno, M. Boyle, L. T. Buchman, L. E. Kidder, H. P. Pfeiffer, and M. A. Scheel, Phys. Rev. D **84**, 124052 (2011).

[46] A. Taracchini, Y. Pan, A. Buonanno, E. Barausse, M. Boyle, T. Chu, G. Lovelace, H. P. Pfeiffer, and M. A. Scheel, Phys. Rev. D **86**, 024011 (2012).

[47] D. McKechan, C. Robinson, and B. Sathyaprakash, Classical Quantum Gravity **27**, 084020 (2010).

[48] C. Loken, D. Gruner, L. Groer, R. Peltier, N. Bunn, M. Craig, T. Henriques, J. Dempsey, C.-H. Yu, J. Chen, L. J. Dursi, J. Chong, S. Northrup, J. Pinto, N. Knecht, and R. V. Zon, J. Phys. Conf. Ser. **256**, 012026 (2010).